

INVERTIBLE MANIFOLD LEARNING FOR DIMENSION REDUCTION

Siyuan Li Haitao Lin Zelin Zang Lirong Wu Jun Xia Stan Z. Li
 School of Engineering, Westlake University &
 Institute of Advanced Technology, Westlake Institute for Advanced Study
 Hangzhou, Zhejiang, China

ABSTRACT

It is widely believed that a nonlinear dimension reduction (NLDR) process drops information inevitably in most practical scenarios, and even with the manifold assumption, most existing methods are unable to preserve structure of data after DR due to the loss of information, especially in high-dimensional cases. In the context of manifold learning, we think a good low-dimensional representation should preserve topological and geometric properties of data manifold. To achieve this, the invertibility of a NLDR transformation is required such that the learned representation is reconstructible via its inverse transformation. In this paper, we propose a novel method, called invertible manifold learning (*inv-ML*), to tackle this problem. A locally isometric smoothness (*LIS*) constraint for preserving local geometry is applied to a two-stage *inv-ML* algorithm. Firstly, a homeomorphic *sparse coordinate transformation* is learned to find the low-dimensional representation without loss of topological information. Secondly, a *linear compression* is performed on the learned sparse coding, with the trade-off between the target dimension and the incurred information loss. Experiments are conducted on seven datasets, whose results demonstrate that the proposed *inv-ML* not only achieves better invertible NLDR in comparison with typical existing methods but also reveals the characteristics of the learned manifolds through linear interpolation in latent space. Moreover, we find that the reliability of tangent space approximated by its local neighborhood on real-world datasets is a key to the success of manifold based DR algorithms. The code will be made available soon.

1 INTRODUCTION

In real-world scenario, it is widely believed that the loss of data information is inevitable after dimension reduction (DR), though the goal of DR is to preserve as much information as possible in the low-dimensional space. In the case of linear DR, compressed sensing (Donoho, 2006) breaks this common sense with practical sparse conditions of the given data. In the case of nonlinear dimension reduction (NLDR), however, it has not been clearly discussed, e.g. what is the structure within data and how to maintain these structure after DR? From the perspective of manifold learning, the *manifold assumption* is widely adopted, but classical manifold based DR algorithms are usually performed not well in the complex practical case. Therefore, what is the gap between theoretical and real-world applications of manifold learning? Here, we give the first detailed discussion of this two problem in the context of manifold learning. We think that a good low-dimensional representation should preserve the topology and geometry of input data, and thus introduce a homeomorphism based invertible NLDR process, combining *sparse coordinate transformation* and *local isometry smoothness* (*LIS*) constraints which preserve the property of topology and geometry, to explain the information-lossless NLDR in manifold learning theoretically. We instantiate the proposed *inv-ML* as a neural network called *i-ML-Enc* via a cascade of equi-dimensional layers and a linear compression layer, and conduct sufficient experiments to validate the invertible DR ability of *i-ML-Enc* and analyze inherent difficulties of classical manifold learning.

Topology preserving dimension reduction. To start, we first make out the definition of information-lossless DR on a manifold. $f : \mathcal{M}_0^d \rightarrow \mathbb{R}^m$ is a smooth mapping of a differential

manifold into another, and if f is a homeomorphism of \mathcal{M}_0^d into $\mathcal{M}_1^d = f(\mathcal{M}_0^d) \subset \mathbb{R}^m$, we call f is an embedding of \mathcal{M}_0^d into \mathbb{R}^m . Assume that the data set $\mathcal{X} = \{\mathbf{x}_j | 1 \leq j \leq n\}$ sampled from the compact manifold $\mathcal{M}_1^d \subset \mathbb{R}^m$ which we call the data manifold and is homeomorphic to \mathcal{M}_0^d . For the sample points we get are represented in the coordinate after inclusion mapping i_1 , we can only regard them as points from Euclidean space \mathbb{R}^m without any prior knowledge. According to the Whitney Embedding Theorem (Seshadri & Verma, 2016), \mathcal{M}_0^d is can be embedded smoothly into \mathbb{R}^{2d} by a homeomorphism g . Rather than to find the $f^{-1} : \mathcal{M}_1^d \rightarrow \mathcal{M}_0^d$, our goal is to seek a smooth map $h : \mathcal{M}_1^d \rightarrow \mathbb{R}^s \subset \mathbb{R}^{2d}$, where $h = g \circ f^{-1}$ is a homeomorphism of \mathcal{M}_1^d into $\mathcal{M}_2^d = h(\mathcal{M}_1^d)$ and $d \leq s \leq 2d \ll m$, and thus the $\dim(h(\mathcal{X})) = s$, which achieves the DR while preserving the topology. Owing to the homeomorphism h we seek as a DR mapping, the data manifold \mathcal{M}_1^d is reconstructible via $\mathcal{M}_1^d = h^{-1} \circ h(\mathcal{M}_1^d)$, by which we mean h a topology preserving DR as well as information-lossless DR.

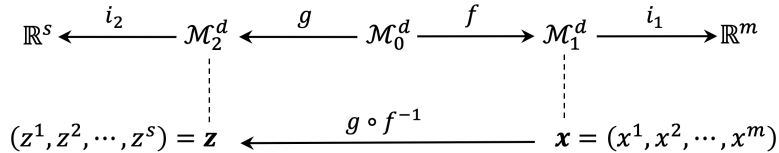


Figure 1: Illustration of the process of NLDR. \mathbf{x} is sampled from \mathcal{M}_1^d and represented in the Euclidean space \mathbb{R}^m after an inclusion mapping i_1 . For the topology preserving dimension reduction methods, it aims to find a homeomorphism $g \circ f^{-1}$ to map \mathbf{x} into \mathbf{z} which is embedded in \mathbb{R}^s .

Geometry preserving dimension reduction. While the topology of the data manifold \mathcal{M}_1^d can be preserved by the homeomorphism h discussed above, it may distort the geometry. To preserve the local geometry of the data manifold, the map should be isometric on the tangent space $\mathcal{T}_p \mathcal{M}_1^d$ for every $p \in \mathcal{M}_1^d$, indicating that $d_{\mathcal{M}_1^d}(u, v) = d_{\mathcal{M}_2^d}(h(u), h(v))$, $\forall u, v \in \mathcal{T}_p \mathcal{M}_1^d$. By Nash’s Embedding Theorem (Nash, 1956), any smooth manifold of class C^k with $k \geq 3$ and dimension d can be embedded isometrically in the Euclidean space \mathbb{R}^s with s polynomial in d .

2 RELATED WORK

Manifold learning. Most classical linear or nonlinear DR methods aim to preserve geometric properties of the manifold. The Isomap (Tenenbaum et al., 2000) based methods aim to preserve the global metric between every pair of sample points. For example, McQueen et al. (2016) can be regarded as such methods based on the push-forward Riemannian metric. For the other aspect, LLE (Roweis & Saul, 2000) based methods try to preserve local geometry after DR, whose derivatives like LTSA (Zhang & Zha, 2004), MLLS (Zhang & Wang, 2007), etc. have been widely used but usually fail in the high-dimensional case. Recently, based on the local properties of manifold, MLDL (Li et al., 2020) has been proposed as a robust locally geometry preserving method implemented by neural network, abandoning the retention of topology. In contrast, our method takes preservation of geometry as well as topology into consideration, trying to maintain these properties of manifolds even in excessive dimension reduction, where the target dimension s' is smaller than s .

Invertible model. From AutoEncoder (AE) (Hinton & Salakhutdinov, 2006), the fundamental neural network based model, having achieved DR and cut information loss by minimizing the reconstruction loss, some AE based generative models like VAE (Kingma & Welling, 2014) and manifold-based NLDR models like TopoAE (Moor et al., 2020) has emerged. These methods cannot avoid information loss after NLDR, and thus, some invertible models consist of a series of equi-dimensional layers have been proposed, some of which aim to generate samples by density estimation through layers (Dinh et al., 2015) (Dinh et al., 2017) (Behrmann et al., 2019), and the other of which are established for other targets, e.g. validating the mutual information bottleneck (Jacobsen et al., 2018). Different from methods mentioned above, our proposed *i-ML-Enc* is a neural network based encoder, with DR as well as maintaining structure of raw data points based on manifold assumption via a series of equi-dimensional layers.

Compressed sensing. The Johnson–Lindenstrauss Theorem (Johnson & Lindenstrauss, 1984) provides the lower bound of target dimension for linear DR with the pairwise distance loss. Given

a small constant $\epsilon \in (0, 1)$ and n samples $\{\mathbf{x}_i\}_{i=1}^n$ in \mathbb{R}^m , a linear projection $W : \mathbb{R}^m \rightarrow \mathbb{R}^s$, $s > O(\frac{\log m}{\epsilon^2})$ can be found, which embeds samples into a s -dimensional space with $(1 + \epsilon)$ distortion of any sample pairs $(\mathbf{x}_i, \mathbf{x}_j)$. It adopts a prior assumption that the given samples in high-dimensional space have a relevant low-dimensional structure constraint which can be maintained by keeping the pairwise distance. Further, compressed sensing (CS) provides strict sparse conditions of linear DR with great probability to recover the compressed signal, which usually cooperates with sparse dictionary learning (Hawe et al., 2013). The core of CS is Restricted Isometry Property (RIP) condition, which reads

$$(1 - \epsilon)\|\mathbf{x}_1 - \mathbf{x}_2\|^2 \leq \|W(\mathbf{x}_1 - \mathbf{x}_2)\|^2 \leq (1 + \epsilon)\|\mathbf{x}_1 - \mathbf{x}_2\|^2, \quad (1)$$

where $\epsilon \in (0, 1)$ is a rather small constant and W is a linear measurement of signal \mathbf{x}_1 and \mathbf{x}_2 . Given a signal $\mathbf{x} \in \mathbb{R}^m$ with s -sparse representation $\alpha = \Phi\mathbf{x}$ on an m -dimensional orthogonal basis Φ , α can be recovered from the linear measurement $\mathbf{y} = W\alpha$ with great probability by the sparse optimization if $W_{m \times s}$ satisfies the RIP condition: $\arg \min_{\tilde{\alpha}} \|\tilde{\alpha}\|_0$, s.t. $\mathbf{y} = W\tilde{\alpha}$. The linear measurement is rewritten as $\mathbf{y} = \Psi\Phi\alpha = \Psi\mathbf{x}$ where Ψ is a low-dimensional orthogonal basis and Φ can be found by the nonlinear dictionary learning. There are some reconstructible CS-based NLDR methods (Wei et al., 2015) (Wei et al., 2019), but their performance is not impressive.

3 PROPOSED METHOD

We will specifically discuss the proposed two-stage NLDR as the first stage in Sec 3.1, in which a s -dimensional representation is learned by a homeomorphism transformation while keeping all topological and geometric structure of the data manifold; then give applicable conditions in real-world scenarios as the second stage in Sec 3.2, in which the dimension is further compressed to s' . We instantiate the proposed DR process as a neural network based on ML-Enc (Li et al., 2020) in Sec 3.3.

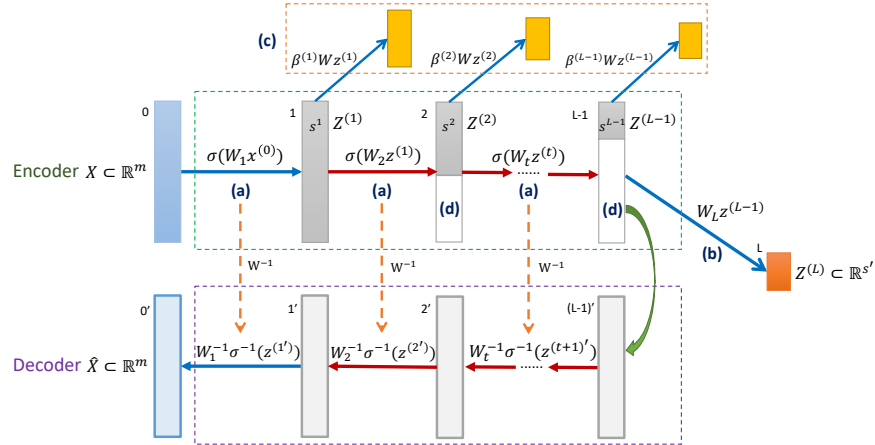


Figure 2: The network structure for the proposed method. The first $L - 1$ layers equi-dimensional mapping in the green box are the first stage which achieves s -sparse and has inverse process in the purple box. (a) is a layer of nonlinear homeomorphism transformation. (b) linearly transforms s -sparse representation in \mathbb{R}^m into $\mathbb{R}^{s'}$ in the second stage. (c) are the *extra heads*. (d) indicates the padding loss of the l -th layer to force $d^{(l)}$ -sparse.

3.1 TOPOLOGY AND GEOMETRY PRESERVATION

Canonical embedding for homeomorphism. To seek the smooth homeomorphism h , we turn to the theorem of local canonical form of immersion (Mei, 2013). Let $f : \mathcal{M} \rightarrow \mathcal{N}$ an immersion, and for any $p \in \mathcal{M}$, there exist local coordinate systems (U, ϕ) around p and (V, ψ) around $f(p)$ such that $\psi \circ f \circ \phi^{-1} : \phi(U) \rightarrow \psi(V)$ is a canonical embedding, which reads

$$\psi \circ f \circ \phi^{-1}(x^1, x^2, \dots, x^d) = (x^1, x^2, \dots, x^d, 0, 0, \dots, 0).$$

In our case, let $\mathcal{M} = \mathcal{M}_2^d$, and $\mathcal{N} = \mathcal{M}_1^d$, any point $\mathbf{z} = (z^1, z^2, \dots, z^s) \in \mathcal{M}_1^d \subset \mathbb{R}^s$ can be mapped to a point in \mathbb{R}^m by the canonical embedding

$$\psi \circ h^{-1}(z^1, z^2, \dots, z^s) = (z^1, z^2, \dots, z^s, 0, 0, \dots, 0). \quad (2)$$

For the point \mathbf{z} is regarded as a point in \mathbb{R}^s , $\phi = \mathbb{I}$ is an identity mapping, and for $h = g \circ f^{-1}$ is a homeomorphism, h^{-1} is continuous. The Eq. 2 can be written as

$$\begin{aligned} (z^1, z^2, \dots, z^s) &= h \circ \psi^{-1}(z^1, z^2, \dots, z^s, 0, 0, \dots, 0) \\ &= h(x^1, x^2, \dots, x^m) \end{aligned}$$

Therefore, to reduce $\dim(\mathcal{X}) = m$ to s , we can decompose h into ψ and $h \circ \psi^{-1}$, by firstly finding a homeomorphic coordinate transformation ψ to map $\mathbf{x} = (x^1, x^2, \dots, x^m)$ into $\psi(\mathbf{x}) = (z^1, z^2, \dots, z^s, 0, 0, \dots, 0)$, which is called a *sparse coordinate transformation*, and $h \circ \psi^{-1}$ can be easily obtained by Eq. 2. We denote $h \circ \psi^{-1}$ by h_0 and call it a *sparse compression*. The theorem holds for any manifold, while in our case, we aims to find the mapping of $\mathcal{X} \subset \mathbb{R}^m$ into \mathbb{R}^s , so the local coordinate systems can be extended to the whole space of \mathbb{R}^m .

Local isometry constraint. The local isometry proposed by MLDL (Li et al., 2020) is employed, imposing the prior LIS constraint, which aims to preserve distances (or some other metrics) locally so that $d_{\mathcal{M}_1^d}(u, v) = d_{\mathcal{M}_2^d}(h(u), h(v)), \forall u, v \in \mathcal{T}_p \mathcal{M}_1^d$.

3.2 LINEAR COMPRESSION

With the former discussed method, manifold-based NLDR can be achieved with topology and geometry preserved, i.e. s -sparse representation in \mathbb{R}^m . However, the target dimension s' may be even less than s , further compression can be performed through the *linear compression* $h'_0: \mathbb{R}^m \rightarrow \mathbb{R}^{s'}$ instead of *sparse compression*, where $h'_0(\mathbf{z}) = W_{m \times s'} \mathbf{z}$, with minor information loss. In general, the *sparse compression* is a particular case of *linear compression* with $h_0(\mathbf{z}) = h'_0(\mathbf{z}) = \Lambda \mathbf{z}$, where $\Lambda = (\delta_{i,j})_{m \times s}$ and $\delta_{i,j}$ is the Kronecker delta. We discusses the information loss caused by a linear compression under different target dimensions s' as following cases.

Theoretical case. In the case of $d \leq s \leq s'$, based on compressed sensing, we can reconstruct the raw input data after NLDR process without loss of any information by solving the sparse optimization problem mentioned in Sec. 2 when the transformation matrix $W_{m \times s'}$ has full rank of column. In the case of $d \leq s' < s$, it is inevitable to drop the topological properties because the two spaces before and after NLDR are not homeomorphic, and it is reduced to local geometry preservation by LIS constraint. However, in the case of $s' \leq d < s$, both topological and geometric information is lost to varying degrees. Therefore, we can only try to retain as much geometric structure as possible.

Practical case. In real-world scenarios, the target dimension s' is usually lower than s , even lower than d . Meanwhile, the data sampling rate is quite low, and clustering effect is extremely significant, indicating it is possible to approximate \mathcal{M}_1 by low-dimensional hyper-plane in the Euclidean space. In the case of $s' < s$, we can retain as the prior Euclidean topological structure as additional topological information of the raw data points.

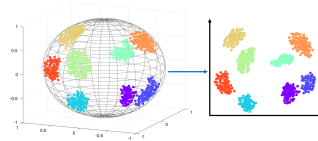


Figure 3: Sparsity and clustering effect.

3.3 NETWORK FOR IMPLEMENTATION

Based on Sec 3.1 and Sec 3.2, we propose a neural network *i-ML-Enc* which achieves two-stage NLDR preserving both topology and geometry, as shown in Fig. 2. In this section, we will introduce the function of network structures and loss functions respectively, including the orthogonal loss, padding loss and *extra heads* for the first stage, and the LIS loss, push-away loss for the second stage.

Cascade of homeomorphisms. Since the *sparse coordinate transformation* ψ (and its inverse) can be highly nonlinear and complex, we decompose it into a cascade of $L-1$ isometric homeomorphisms $\psi = \psi^{(L-1)} \circ \dots \circ \psi^{(2)} \circ \psi^{(1)}$, which can be achieved by $L-1$ equi-dimensional network layers. For each $\psi^{(l)}$, it is a *sparse coordinate transformation*, where $\psi^{(l)}(z^{1,(l)}, z^{2,(l)}, \dots, z^{s_l,(l)}, 0, \dots, 0) =$

$(z^{1,(l+1)}, z^{2,(l+1)}, \dots, z^{s_{l+1},(l+1)}, 0, \dots, 0)$ with $s_{l+1} < s_l$ and $s_{L-1} = s$. The layer-wise transformation $Z^{(l+1)} = \psi^{(l)}(Z^{(l)})$ and its inverse can be written as

$$Z^{(l+1)} = \sigma(W_l X^{(l)}), \quad Z^{(l)'} = W_l^{-1}(\sigma^{-1}(Z^{(l+1)'})), \quad (3)$$

in which W_l is the l -th weight matrix of the neural network to be learned, and $\sigma(\cdot)$ is a nonlinear activation. The bias term is removed here to facilitate its simple inverse structure.

Orthogonal loss. Each layer-wise transformation is thought to be a homeomorphism between $Z^{(l)}$ and $Z^{(l+1)}$, and we want it to be a nearly isometric. We force each W_l to be an orthogonal matrix, which allows simple calculation of the inverse of W_l . Based on RIP condition, the orthogonal constraint of the weight matrix in the first $L - 1$ layers can be obtained as

$$L_{orth} = \sum_{l=1}^{L-1} \alpha^{(l)} \rho(W_l^T W_l - I),$$

where $\{\alpha^{(l)}\}$ are the loss weights. Notice that $\rho(W) = \sup_{z \in \mathbb{R}^m, z \neq 0} \frac{|Wz|}{|z|}$ is the spectral norm of W , and the loss term can be written as $\rho(W_l^T W_l - I) = \sup_{z \in \mathbb{R}^m, z \neq 0} \left| \frac{|Wz|}{|z|} \right|$ which is equivalent to RIP condition.

Padding loss. To force sparsity from the second to $(L - 1)$ -th layers, we add a zero padding loss to each of these layers. For the l -th layer whose target dimension is s_l , pad the last $m - s_l$ elements of $z^{(l+1)}$ with zeros and panish these elements with L_1 norm loss:

$$L_{pad} = \sum_{l=2}^{L-1} \beta^{(l)} \sum_{i=s^{(l)}}^m |z_i^{(l+1)}|,$$

where $\{\beta^{(l)}\}$ are loss weights. The target dimension s_l can be set heuristically.

Linear transformation head. We use the linear transformation head to achieve the linear compression step in our NLDR process, which is a transformation between the orthogonal basis of high dimension and lower dimension. Thus, we apply the row orthogonal constraint to W_L .

LIS loss. Since the linear DR is applied at the end of the NLDR process, we apply LIS constraint to preserve the local geometric properties. Take the LIS loss in the l -th layer as an example:

$$L_{LIS}(\psi) = \sum_{i=1}^n \sum_{j \in \mathcal{N}_i^k} \|d_X(\mathbf{x}_i, \mathbf{x}_j) - d_Z(h(\mathbf{x}_i), h(\mathbf{x}_j))\|,$$

where \mathcal{N}_i^k is the set of x_i 's k -nearest neighborhood.

Push-away loss. In the real case discussed in Sec 3.2, the latent space of the $(L - 1)$ -th layer can approximately to be a hyper-plane in Euclidean space, so that we introduce push-away loss to repel the non-adjacent sample points of each x_i in its B -radius neighbourhood in the latent space. It deflates the manifold locally when acting together with L_{LIS} . Similarly, L_{push} is applied after the linear transformation in the L -th layer:

$$L_{push} = - \sum_{i=1}^n \sum_{j \in \mathcal{N}_i^k} \mathbf{1}_{d_Z(h(\mathbf{x}_i^{(l)}), h(\mathbf{x}_j^{(l)})) < B} \log \left(1 + d_Z(h(\mathbf{x}_i^{(l)}), h(\mathbf{x}_j^{(l)})) \right).$$

Extra heads. In order to force the first $L - 1$ layers of the network to achieve NLDR gradually, we introduce auxiliary DR branches, called *extra head*, at layers from the second to the $(L - 1)$ -th. The structure of each *extra head* is same as the linear transformation head and will be discarded after training. L_{extra} is written as

$$L_{extra} = \sum_{l=1}^{L-1} \gamma^{(l)} (L_{LIS} + \mu^{(l)} L_{push}),$$

where $\{\gamma^{(l)}\}$ and $\{\mu^{(l)}\}$ are loss weights which can be set based on $\{s_l\}$.

Inverse process. The inverse process is the decoder directly obtained by the first $L - 1$ layers of the encoder given by Eq. 3, which does not involved in the training process. When the target dimension s' is equal to s , the inverse of the layer- L can be solved by compressed sensing rather than pseudo-inverse.

4 EXPERIMENT

To evaluate the invertibility of *i-ML-Enc* and analyze the property of data manifolds, we carry out experiments on **seven datasets**: (i) Swiss roll (Pedregosa et al., 2011), (ii) Spheres (Moor et al., 2020) and Half Spheres, (iii) USPS (Hull, 1994), (iv) MNIST (LeCun et al., 1998), (v) KMNIST (Clanuwat et al., 2018), (vi) FMNIST (Xiao et al., 2017), (vii) COIL-20 (Nene et al., 1996b). The implementation is based on the PyTorch 1.3.0 library running on NVIDIA v100 GPU.

4.1 METHODS COMPARISON

We compare the proposed *i-ML-Enc* with several typical methods in NLDR and inverse scenarios on Swiss roll, Spheres and Half Spheres, USPS, MNIST, FMNIST and COIL-20 datasets. **Six methods for manifold learning**: MLE (Zhang & Wang, 2007), t-SNE (Maaten & Hinton, 2008) and ML-Enc (Li et al., 2020) are compared for NLDR; three AE-based methods VAE (Kingma & Welling, 2014), TopoAE (Moor et al., 2020) and ML-AE (Li et al., 2020) are compared for reconstructible manifold learning. **Three methods for inverse models**: INN (Nguyen et al., 2019), i-RevNet (Jacobsen et al., 2018), and i-ResNet (Behrmann et al., 2019) are compared for bijective property. Among them, i-RevNet and i-ResNet are supervised algorithms while the rest are unsupervised. **Hyperparameter** values of *i-ML-Enc* and configurations of these datasets such as the input and target dimension are provided in **Appendix A.2**.

Table 1: Comparison in representation and invertible quality on MNIST datasets

Dataset	Algorithm	RMSE	MNE	Trust	Cont	K min	K max	l -MSE	Acc
MNIST	MLLE	-	-	0.6709	0.6573	1.873	6.7e+9	36.80	0.8341
	t-SNE	-	-	0.9896	0.9886	5.156	324.9	48.07	0.9246
	ML-Enc	-	-	0.9862	0.9927	1.761	58.91	18.98	0.9326
	VAE	0.5263	33.17	0.9712	0.9703	5.837	130.5	22.79	0.8652
	TopoAE	0.5178	31.45	0.9915	0.9878	4.943	265.3	24.98	0.8993
	ML-AE	0.4012	16.84	0.9893	0.9926	1.704	57.48	19.05	0.9340
	i-ML-Enc (L)	0.0457	0.5085	0.9906	0.9912	2.033	60.14	18.16	0.9316
	INN	0.0615	0.5384	0.9851	0.9823	1.875	22.38	7.494	0.9176
	i-RevNet	0.0443	0.4679	0.9118	0.8785	13.41	142.5	6.958	0.9901
	i-ResNet	0.0502	0.6422	0.9149	0.8922	1.876	19.28	10.78	0.9925
i-ML-Enc(L-1)	0.0407	0.5085	0.9986	0.9973	1.256	5.201	5.895	0.9580	

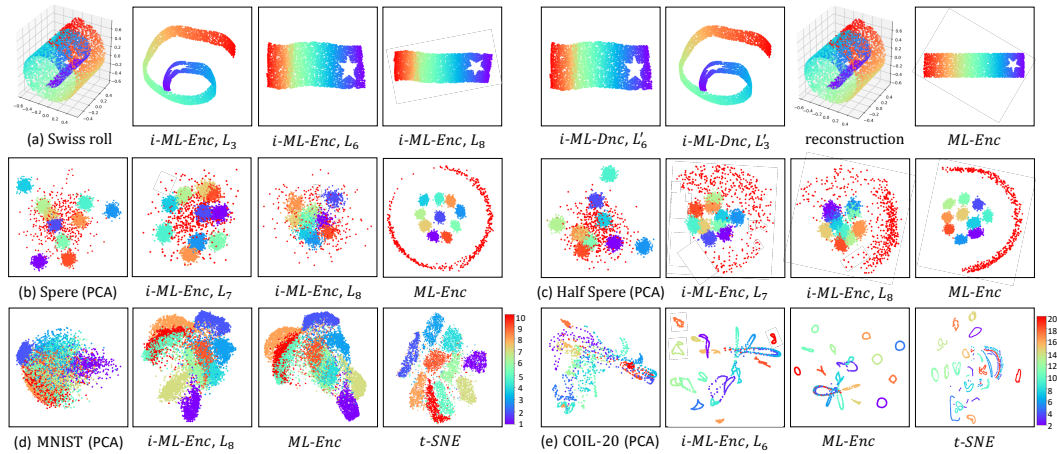


Figure 4: Visualization of invertible NLDR results of *i-ML-Enc* compared to ML-Enc and t-SNE. (a) shows the NLDR and its inverse process of on test set of Swiss roll with the target dimension $s' = 2$; (b) shows the failure case of reducing 101-D Spheres S^{100} into 10-D, while (c) shows DR of 101-D half spheres S^{10} with $s' = 10$; (d) and (e) show results of the relatively dense case on MNIST and sparse case on COIL-20 with $s' = 2$. The high-dimensional results are visualized by PCA.

Evaluation metrics. We evaluate the proposed invertible NLDR algorithm from three aspects: (1) Invertible property. Reconstruction MSE (**RMSE**) and maximum norm error (**MNE**) measure the difference between the input and reconstruction results by norm-based errors. (2) NLDR quality. Trustworthiness (**Trust**) and Continuity (**Cont**) (Moor et al., 2020), latent MSE (**I-MSE**), Minimum (**Kmin**) and Maximum (**Kmax**) local Lipschitz constant (Li et al., 2020) are used to evaluate the quality of the low-dimensional representation. (3) Generalization ability of the representation. Mean accuracy (**Acc**) of linear classification on the representation measures models’ generalization ability to downstream tasks. Their exact definitions and purpose are given in **Appendix A.1**.

Conclusion. Table 1 compares the *i-ML-Enc* with the related methods on MNIST, more detailed analysis and results on Swiss roll, Half Spheres, USPS, FMNIST and COIL-20 are given in **Appendix A.2**. Compared with NLDR algorithms, the L -th layer of *i-ML-Enc* achieves second best NLDR results while preserving the all information of the dataset manifold in the $(L - 1)$ -th layer. Compared with inverse models, *i-ML-Enc* nearly outperforms the other methods in both invertible and NLDR metrics, which indicates that good low-dimensional representation of manifolds can be learned by the equi-dimensional layers. The NLDR and its inverse process of *i-ML-Enc* are visualized in Fig. 4.

4.2 LATENT SPACE INTERPOLATION

Since the first $L - 1$ layers of *i-ML-Enc* are nearly homeomorphism, we carry out linear interpolation experiments on the discrete data points in both the input space and the $(L - 1)$ -th layer latent space to approximate the intrinsic continuous manifold, and verify the latent results by its inverse process. A good low-dimensional representation of the manifold shall not only preserves the local properties, but also is flatter and denser with lower curvature. Thus, we expect that the local linear interpolation results in the latent space should be more reliable than in the input space. The complexity of data manifolds increases from USPS(256), MNIST(256), MNIST(784), KMNIST(784) to FMNIST(784), which is analyzed in **Appendix A.3.1**.

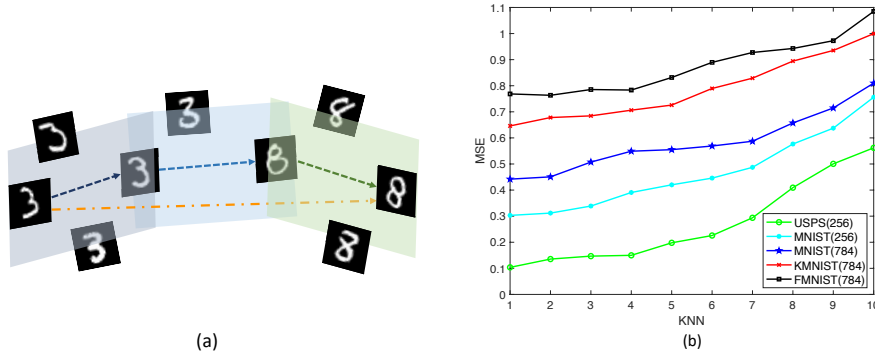


Figure 5: (a) shows the proposed geodesics interpolation on a manifold; (b) reports the MSE loss of 1 to 10 nearest neighbors interpolation results on interpolation datasets.

K-nearest neighbor interpolation. We first verify the reliability of the low-dimensional representation in a small local system by kNN interpolation. Given a sample x_i , randomly select x_j in x_i ’s k-nearest neighborhood in the latent space to form a sample pair (x_i, x_j) . Perform linear interpolation of the latent representation of the pair and get reconstruction results for evaluation as: $\hat{x}_{i,j}^t = \psi^{-1}(t\psi(x_i) + (1 - t)\psi(x_j))$, $t \in [0, 1]$. The experiment is performed on *i-ML-Enc* with $L = 6$ and $K = 15$, training with 8000 samples for USPS and MNIST(256), 20000 samples for MNIST(784), KMNIST, FMNIST.

Evaluation. (1) Calculate the MSE loss between reconstruction results of the latent interpolation $\hat{x}_{i,j}^t$ and the input space result $x_{i,j}^t$, which is the corresponding interpolation results in the local neighborhood of the input space with $x_{i,j}^t = tx_i + (1 - t)x_j$. Fig. 5 shows the results of $k = 1, 2, \dots, 10$. (2) Visualize the typical results of the input space and the latent space for comparison, as shown in Fig. 6. More results and detailed analysis are given in **Appendix A.3.2**.

Geodesic interpolation. Based on 4.2.1, we further employ a more reasonable method to generate the sampling points between two distant samples pairs in the latent space. Given a sample pair (x_i, x_j)

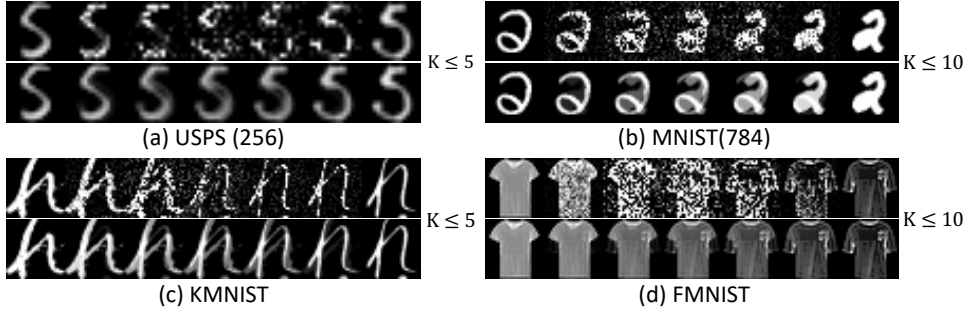


Figure 6: The results of kNN interpolation in latent space. For each dataset, the upper row shows the latent result, while the lower shows the input result. The latent results show more noise but less overlapping and pseudo-contour than the input results.

with $k \geq 45$ from different clusters, we select the three intermediate sample pairs (x_i, x_{i_1}) , (x_{i_1}, x_{i_2}) , (x_{i_2}, x_j) with $k \leq 20$ along the geodesic path in latent space for piece-wise linear interpolation in both space. Visualization results are given in **Appendix A.3.2**.

Conclusion. Compared with results of the kNN and geodesic interpolation, we can conclude: (1) Because of the sparsity of the high-dimensional latent space, noises are inevitable on the latent results indicating the limitation of linear approximation. Empirically, the reliability of the latent interpolation decreases with the expansion of the local neighborhood on the same dataset. (2) We will get worse latent results in the following cases: on the similar manifolds, the sampling rate is lower or the input dimension is higher indicated by USPS(256), MNIST(256) and MNIST(784); with the same sampling rate and input dimension, the manifold is more complex indicated by MNIST(784), KMNIST to FMNIST. They indicate that the confidence of the tangent space estimated by local neighborhood decreases on more complex manifolds with sparse sampling. (3) The interpolation between two samples in latent space is smoother than that in the input space, validating the flatness and density of the lower-dimensional representation learned by *i-ML-Enc*. Overall, we infer that the unreliable approximation of the local tangent space by the local neighborhood is the basic reason for the manifold learning fails in the real-world case, because the geometry should be preserved in the first place. To come up with this common situation, it is necessary to import other prior assumption or knowledge when the sampling rate of the data manifold is quite low, e.g. the Euclidean space assumption, semantic information of down-stream tasks.

4.3 ABLATION STUDY

We perform ablation study on MNIST, USPS, KMNIST, FMNIST and COIL-20 to evaluate effects of the network structure and the loss terms in *i-ML-Enc* for manifold learning and invertible property. Based on ML-Enc, three proposed parts are added: the *extra head* (**Ex**), the orthogonal loss \mathcal{L}_{orth} (**Orth**), the zero padding loss \mathcal{L}_{pad} (**Pad**). Besides the previous 8 indicators, we introduce the rank of the output matrix of the layer $L - 1$ as $r(Z^{L-1})$, to measure the sparsity of the high-dimensional representation. We conclude that the **Ex+Orth+Pad** is the best combination to achieve invertible NLDR with s -sparse, e.g. 125-sparse on MNIST. The detailed analysis of experiment results and further discussion of the s -sparse are given in **Appendix A.4**.

5 CONCLUSION

A novel invertible DR process *inv-ML* and a neural network implementation *inv-ML-Enc* are proposed to tackle two problems of manifold-based DR in practical scenarios, i.e., the condition for information-lossless NLDR and the key issue of manifold learning. Firstly, the *sparse coordinate transformation* is learned to find a flatter and denser low-dimensional representation with preservation of geometry and topology of data manifolds. Secondly, we discuss the information loss with different target dimensions in *linear compression*. Experiment results of *i-ML-Enc* on seven datasets validate its invertibility. Further, the interpolation experiments reveal that finding a reliable tangent space by the local neighborhood on real-world datasets is the inherent defect of manifold based DR methods.

REFERENCES

- Jens Behrmann, Will Grathwohl, Ricky T. Q. Chen, David Duvenaud, and Jörn-Henrik Jacobsen. Invertible residual networks. In *Proceedings of the 36th International Conference on Machine Learning (ICML)*, Proceedings of Machine Learning Research, pp. 573–582, 2019.
- Tarin Clanuwat, Mikel Bober-Irizar, Asanobu Kitamoto, Alex Lamb, Kazuaki Yamamoto, and David Ha. Deep learning for classical japanese literature. *arXiv preprint arXiv:1812.01718*, 2018. URL <http://arxiv.org/abs/1812.01718>.
- Laurent Dinh, David Krueger, and Yoshua Bengio. NICE: non-linear independent components estimation. In *3rd International Conference on Learning Representations (ICLR)*, 2015. URL <http://arxiv.org/abs/1410.8516>.
- Laurent Dinh, Jascha Sohl-Dickstein, and Samy Bengio. Density estimation using real NVP. In *5th International Conference on Learning Representations (ICLR)*. OpenReview.net, 2017. URL <https://openreview.net/forum?id=HkpbnH91x>.
- David L. Donoho. Compressed sensing. *IEEE Trans. Inf. Theory*, 52:1289–1306, 2006.
- Simon Hawe, Matthias Seibert, and Martin Kleinsteuber. Separable dictionary learning. In *IEEE Conference on Computer Vision and Pattern Recognition (CVPR)*, pp. 438–445. IEEE Computer Society, 2013.
- Matthias Hein and Jean-Yves Audibert. Intrinsic dimensionality estimation of submanifolds in \mathbb{R}^d . pp. 289–296, 2005.
- Geoffrey E Hinton and Ruslan R Salakhutdinov. Reducing the dimensionality of data with neural networks. *science*, 313(5786):504–507, 2006.
- Jonathan Hull. Database for handwritten text recognition research. *IEEE Transactions on Pattern Analysis and Machine Intelligence*, 16:550 – 554, 05 1994. doi: 10.1109/34.291440.
- Jörn-Henrik Jacobsen, Arnold W. M. Smeulders, and Edouard Oyallon. i-revnet: Deep invertible networks. In *Proceedings of 6th International Conference on Learning Representations (ICLR)*. OpenReview.net, 2018.
- William B. Johnson and JohnsonJoram Lindenstrauss. Extensions of lipschitz maps into a hilbert space. *Contemporary Mathematics*, 26:189–206, 01 1984.
- Diederik P. Kingma and Jimmy Ba. Adam: A method for stochastic optimization. In *Proceedings of 3rd International Conference on Learning Representations (ICLR)*, 2015. URL <http://arxiv.org/abs/1412.6980>.
- Diederik P. Kingma and Max Welling. Auto-encoding variational bayes. In *2nd International Conference on Learning Representations (ICLR)*, 2014.
- Yann LeCun, Léon Bottou, and Patrick Haffner. Gradient-based learning applied to document recognition. *Proceedings of the IEEE*, 86(11):2278–2324, 1998.
- Stan Z. Li, Zelin Zhang, and Lirong Wu. Markov-lipschitz deep learning. *arXiv preprint arXiv:2006.08256*, abs/2006.08256, 2020. URL <https://arxiv.org/abs/2006.08256>.
- Laurens van der Maaten and Geoffrey Hinton. Visualizing data using t-sne. *Journal of machine learning research*, 9(Nov):2579–2605, 2008.
- James McQueen, Marina Meila, and Dominique Joncas. Nearly isometric embedding by relaxation. In *Proceedings of the 29th Neural Information Processing Systems (NIPS)*, pp. 2631–2639, 2016.
- Jiaqiang Mei. *Introduction to Manifold and Geometry*. Beijing Science Press, 2013.
- Michael Moor, Max Horn, Bastian Rieck, and Karsten Borgwardt. Topological autoencoders. In *Proceedings of the 37th International Conference on Machine Learning (ICML)*, Proceedings of Machine Learning Research, 2020.

- John Nash. The imbedding problem for riemannian manifolds. *Annals of Mathematics*, 63:20–63, 1956.
- Sameer Nene, Shree Nayar, and H. Murase. Columbia object image library (coil-100). Technical report, Columbia University, 03 1996a. URL <https://www.cs.columbia.edu/CAVE/software/softlib/coil-20.php>.
- Sameer A. Nene, Shree K. Nayar, and Hiroshi Murase. Columbia object image library (coil-20). Technical report, Columbia University, 1996b. URL <https://www.cs.columbia.edu/CAVE/software/softlib/coil-20.php>.
- The-Gia Leo Nguyen, Lynton Ardizzone, and Ullrich Köthe. Training invertible neural networks as autoencoders. In *Proceedings of 41st German Conference of Pattern Recognition (GCPR)*, volume 11824, pp. 442–455. Springer, 2019.
- Fabian Pedregosa, Gaël Varoquaux, Alexandre Gramfort, Vincent Michel, Bertrand Thirion, Olivier Grisel, Mathieu Blondel, Peter Prettenhofer, Ron Weiss, Vincent Dubourg, Jake Vanderplas, Alexandre Passos, David Cournapeau, Matthieu Brucher, Matthieu Perrot, and Édouard Duchesnay. Scikit-learn: Machine learning in python. *Journal of Machine Learning Research*, 12(85):2825–2830, 2011. URL <http://jmlr.org/papers/v12/pedregosa11a.html>.
- Sam T Roweis and Lawrence K Saul. Nonlinear dimensionality reduction by locally linear embedding. *science*, 290:2323–2326, 2000.
- Harish Seshadri and Kaushal Verma. The embedding theorems of whitney and nash. *Resonance*, pp. 815—826, 2016.
- Joshua B Tenenbaum, Vin De Silva, and John C Langford. A global geometric framework for nonlinear dimensionality reduction. *science*, 290(5500):2319–2323, 2000.
- Xian Wei, Martin Kleinsteuber, and Hao Shen. Invertible nonlinear dimensionality reduction via joint dictionary learning. In *12th Latent Variable Analysis and Signal Separation (LVA/ICA)*, volume 9237 of *Lecture Notes in Computer Science*, pp. 279–286. Springer, 2015.
- Xian Wei, Hao Shen, Yuanxiang Li, Xuan Tang, Fengxiang Wang, Martin Kleinsteuber, and Yi Lu Murphey. Reconstructible nonlinear dimensionality reduction via joint dictionary learning. *IEEE Trans. Neural Networks Learn. Syst.*, 30(1):175–189, 2019.
- Han Xiao, Kashif Rasul, and Roland Vollgraf. Fashion-mnist: a novel image dataset for benchmarking machine learning algorithms. *arXiv preprint arXiv:1708.07747*, 2017. URL <http://arxiv.org/abs/1708.07747>.
- Zhenyue Zhang and Jing Wang. Mlle: Modified locally linear embedding using multiple weights. In *Advances in Neural Information Processing systems*, pp. 1593–1600, 2007.
- Zhenyue Zhang and Hongyuan Zha. Principal manifolds and nonlinear dimensionality reduction via tangent space alignment. *SIAM journal on scientific computing*, 26(1):313–338, 2004.

A APPENDIX

A.1 DEFINITIONS OF PERFORMANCE METRICS

As for NLDR tasks, We adopt the performance metrics used in MLDL (Li et al., 2020) and TopoAE (Moor et al., 2020) to measure topology-based manifold learning, and add a new indicator to evaluate the generalization ability of the latent space. Essentially, the related indicators regard the local neighborhood of the input space as the ground truth. As for the invertible property, we adopted the norm-based reconstruction metrics, i.e. the L_2 and L_∞ norm errors, which are also based on the inputs. The following notations are used in the definitions $d_{i,j}^{(l)}$ is the pairwise distance in space $Z^{(l)}$; $\mathcal{N}_{i,k}^{(l)}$ is the set of indices to the k -nearest neighbors (k -NN) of $z_i^{(l)}$ in latent space, and $\mathcal{N}_{i,k}$ is the set of indices to the k -NN of x_i in input space; $r_{i,j}^{(l)}$ is the closeness rank of $z_j^{(l)}$ in the k -NN of $z_i^{(l)}$. The evaluation metrics are defined below:

- (1) **RMSE** (invertible quality). This indicator is commonly used to measure reconstruction quality. Based on the input x and the reconstruction output \hat{x} , the mean square error (MSE) of the L_2 norm is defined as:

$$RMSE = \left(\frac{1}{N^2} \sum_{i=1}^N (x_i - z_i)^2 \right)^{\frac{1}{2}}.$$

- (2) **MNE** (invertible quality). This indicator is designed to evaluate the bijective property of a L layers neural network model. Specifically, taking each invertible unit in the network, calculate the L_∞ norm error of the input and reconstruction output of each corresponding layer, and choose the maximum value among all units. If a model is bijective, this indicator can reflect the stability of the model:

$$MNE = \max_{1 \leq l \leq L-1} \|z_l - \hat{z}_l\|_\infty, \quad l = 1, 2, \dots, L.$$

- (3) **Trust** (embedding quality). The indicator measures how well neighbors are preserved between the two spaces. The k nearest neighbors of a point are preserved when going from the input space X to space $Z^{(l)}$:

$$Trust = \frac{1}{k_2 - k_1 + 1} \sum_{k=k_1}^{k_2} \left\{ 1 - \frac{2}{Mk(2M - 3k - 1)} \sum_{i=1}^M \sum_{j \in \mathcal{N}_{i,k}^{(l)}, j \notin \mathcal{N}_{i,k}} (r_{i,j}^{(l)} - k) \right\}$$

where k_1 and k_2 are the bounds of the number of nearest neighbors, so averaged for different k -NN numbers.

- (4) **Cont** (embedding quality). The indicator is asymmetric to **Trust** (from space $Z^{(l)}$ to space X):

$$Cont = \frac{1}{k_2 - k_1 + 1} \sum_{k=k_1}^{k_2} \left\{ 1 - \frac{2}{Mk(2M - 3k - 1)} \sum_{i=1}^M \sum_{j \in \mathcal{N}_{i,k}, j \notin \mathcal{N}_{i,k}^{(l)}} (r_{i,j}^{(l)} - k) \right\}$$

- (5) **Kmin** and **Kmax** (embedding quality). Those indicators are the minimum and maximum of the local bi-Lipschitz constant for the homeomorphism between input space and the l -th layer, with respect to the given neighborhood system:

$$K_{\min} = \min_{1 \leq i \leq M} \max_{j \in \mathcal{N}_{i,k}^{(l)}} K_{i,j}, \quad K_{\max} = \max_{1 \leq i \leq M} \max_{j \in \mathcal{N}_{i,k}^{(l)}} K_{i,j},$$

where k is that for k -NN used in defining \mathcal{N}_i and

$$K_{i,j} = \max \left\{ \frac{d_{i,j}^{(l)}}{d_{i,j}^{(l')}}, \frac{d_{i,j}^{(l')}}{d_{i,j}^{(l)}} \right\}.$$

- (6) ***l*-MSE** (embedding quality). This indicator is to evaluate the distance disturbance between the input space and latent space with L_2 norm-based error.

$$l_{MSE} = \left(\frac{1}{N^2} \sum_{i=1}^N \sum_{j=1}^N \|d_X(\mathbf{x}_i, \mathbf{x}_j) - d_Z(h(\mathbf{x}_i), h(\mathbf{x}_j))\| \right)^{\frac{1}{2}}.$$

- (7) **ACC** (generalization ability). To measure the generalization ability of the learned representation, logistic regression (Pedregosa et al., 2011) is performed after the latent representation. We report the mean accuracy on the test set for 10-fold cross-validation.

A.2 METHOD COMPARISON

Configurations of datasets. The NLDR performance and its inverse process are verified on both synthetic and real world datasets. As shown in Table 2, we list the **type** of the dataset, the **class** number of clusters, the **input** dimension m , the **target** dimension s' , the **intrinsic** dimension d which is only an approximation for the real world dataset, the sample number of **train** and **test**, and the **logistic** classification performance on the latent representation. Among them, Swiss roll serves as an ideal example of information-lossless NLDR; Spheres serves as an excessive case of NLDR compared to half spheres; four image datasets with increasing difficulties are used to analyze complex situations in real world scenarios. Besides, the lower bound and upper bound of the intrinsic dimension of real-world datasets are approximated by (Hein & Audibert, 2005) and AE-based INN (Nguyen et al., 2019). Specifically, the upper bound can be found the grid search of different bottlenecks of the INN, and we report the bottleneck size of each dataset when the reconstruction MSE loss is almost unchanged.

Table 2: Brief introduction to the configuration of datasets for method comparison.

Dataset	Type	Class	Input m	Target s'	intrinsic d	Train	Test	Logistic
Swiss roll	synthetic	-	3	2	2	800	8000	-
Spheres	synthetic	-	101	10	101	5500	5500	-
Half spheres	synthetic	-	101	10	10	5500	5500	-
USPS	real world	10	256	10	10 to 80	4649	4649	0.9381
MNIST	real world	10	784	10	10 to 100	20000	10000	0.8943
FMNIST	real world	10	784	10	20 to 140	20000	10000	0.7984
COIL-20	real world	20	4096	20	20 to 260	1440	1440	0.9974

Hyperparameter values. Basically, we set $\alpha = 0.1$ in LeakyReLU, and optimize the *i-ML-Enc* with Adam (Kingma & Ba, 2015) for 10000 epochs. We set the hyperparameter based on two intuitions: (1) the implementation of *sparse coordinate transformation* should achieve DR on the premise of maintaining homeomorphism; (2) NLDR should be achieved gradually rather than suddenly. Based on (1), we gradually decrease the *extra heads* weights γ linearly for epochs from 2000 to 8000, while linearly increase the orthogonal loss weights α for epochs from 500 to 2000. Based on (2), we approximate the DR trend by exponential series. For the *extra heads*, the target dimension s^l should decrease exponentially from m to s' for the 2-th to $(L - 1)$ -th layer, and the push-away loss weights μ decrease linearly. Similarly, the padding weight β should increase linearly. The layer number L is set to 6 for COIL-20, and 8 for other datasets.

Results on toy datasets. The Table 3 compares the *i-ML-Enc* with other methods in 9 performance metrics on Swiss roll and half spheres. Seven methods for manifold learning: t-SNE (Maaten & Hinton, 2008), RR (McQueen et al., 2016) and ML-Enc (Li et al., 2020) are compared for NLDR; four AE-based methods AE (Hinton & Salakhutdinov, 2006), VAE (Kingma & Welling, 2014), TopoAE (Moor et al., 2020), and ML-AE (Li et al., 2020) are compared for reconstructible manifold learning. We report the L -th layer of *i-ML-Enc* for the NLDR quality and the $(L - 1)$ -th layer for the invertible ability. ML-Enc performs best in Trust, K min, K max and *l*-MSE on Swiss roll which shows its great NLDR ability in the low-dimensional case, while *i-ML-Enc* shows advantages in the high-dimensional case. It shows that *i-ML-Enc* outperforms other methods in its invertible property of the $(L - 1)$ -th layer.

Table 3: Comparison in embedding and invertible quality on Swiss Roll and Half-Sphere datasets

Dataset	Algorithm	RMSE	MNE	Trust	Cont	K min	K max	l -MSE
Swiss Roll	t-SNE	-	-	0.9987	0.9843	10.96	1097	3.407
	RR	-	-	0.9286	0.9847	4.375	187.7	0.0453
	ML-Enc	-	-	0.9999	0.9985	1.000	2.141	0.0039
	AE	0.3976	10.55	0.8724	0.8333	1.687	4230	0.0308
	VAE	0.7944	13.97	0.5064	0.6486	1.51	4809	0.0397
	TopoAE	0.5601	11.61	0.9198	0.9881	1.194	220.6	0.1165
	ML-AE	0.0208	8.134	0.9998	0.9847	1.005	2.462	0.0051
i-ML-Enc (L)	0.0048	0.0649	0.9996	0.9986	1.004	2.471	0.0043	
Half Sphere	t-SNE	-	-	0.8908	0.9278	25.33	790.9	2.6665
	RR	-	-	0.8643	0.8516	3.047	201.2	0.4789
	ML-Enc	-	-	0.8837	0.9305	1.029	46.35	0.0207
	AE	0.7359	11.54	0.6886	0.7069	1.763	4112	0.0808
	VAE	0.8474	14.97	0.5398	0.6197	2.361	4682	0.1205
	TopoAE	0.9174	13.68	0.8574	0.8226	1.375	154.8	0.4342
	ML-AE	0.6339	9.492	0.8819	0.9293	1.025	43.17	0.0218
	i-ML-Enc (L)	0.1095	0.7985	0.8892	0.9295	1.491	41.25	0.0463

Table 4: Comparison in embedding and invertible quality on USPS, FMNIST and COIL-20 datasets

Dataset	Algorithm	RMSE	MNE	Trust	Cont	K min	K max	l -MSE	Acc
USPS	t-SNE	-	-	0.9831	0.9889	3.238	194.8	35.53	0.9522
	ML-Enc	-	-	0.9874	0.9897	1.562	52.14	14.88	0.9534
	AE	0.6201	29.09	0.9845	0.974	4.728	87.41	17.41	0.8952
	TopoAE	0.647	30.19	0.9830	0.9852	3.598	126.2	19.98	0.8876
	ML-AE	0.4912	11.84	0.9879	0.9905	1.529	55.32	15.05	0.9576
	i-ML-Enc (L)	0.0253	0.3058	0.9886	0.9861	1.487	60.79	15.16	0.9435
	INN	0.0535	0.5239	0.9872	0.9843	1.795	26.38	9.581	0.9305
	i-RevNet	0.0337	0.3471	0.9187	0.9096	11.25	183.2	6.209	0.9945
	i-ResNet	0.0437	0.5789	0.9205	0.9122	1.635	18.375	9.875	0.9974
i-ML-Enc(L-1)	0.0253	0.3058	0.9934	0.9927	1.165	4.974	5.461	0.9876	
FMNIST	t-SNE	-	-	0.9896	0.9863	3.247	108.3	48.07	0.7249
	ML-Enc	-	-	0.9903	0.9896	1.358	89.65	25.18	0.7629
	AE	0.2078	27.45	0.9744	0.9689	6.728	102.1	21.98	0.7495
	TopoAE	0.2236	31.01	0.9658	0.9813	6.982	115.4	23.53	0.7503
	ML-AE	0.4912	18.84	0.9912	0.9917	1.738	101.7	25.89	0.7665
	i-ML-Enc (L)	0.0461	0.3567	0.9923	0.9905	1.295	83.63	20.13	0.7644
	INN	0.0627	0.6819	0.9832	0.9744	1.364	21.36	9.258	0.8471
	i-RevNet	0.0475	0.3519	0.9157	0.8967	21.58	204.8	6.517	0.9386
	i-ResNet	0.0582	0.6719	0.9242	0.9058	1.953	22.75	9.687	0.9477
i-ML-Enc(L-1)	0.0461	0.3567	0.9935	0.9959	1.356	6.704	6.017	0.8538	
Coil-20	t-SNE	-	-	0.9911	0.9954	5.794	101.2	17.22	0.9039
	ML-Enc	-	-	0.9920	0.9889	1.502	70.79	9.961	0.9564
	AE	0.3507	24.09	0.9745	0.9413	4.524	85.09	11.45	0.8958
	TopoAE	0.4712	26.66	0.9768	0.9625	5.272	98.33	27.19	0.9043
	ML-AE	0.1220	16.86	0.9914	0.9885	1.489	68.63	10.34	0.9548
	i-ML-Enc (L)	0.0312	1.026	0.9921	0.9871	1.695	71.86	11.13	0.9386
	INN	0.0758	0.8075	0.9791	0.9681	2.033	79.25	8.595	0.9936
	i-RevNet	0.0508	0.7544	0.9316	0.9278	11.34	147.2	9.803	1.000
	i-ResNet	0.0544	0.7391	0.9258	0.9136	1.821	13.56	10.41	1.000
i-ML-Enc(L-1)	0.0312	0.9263	0.9940	0.9937	1.297	4.439	7.539	1.000	

Results on real-world datasets. The Table 4 compares the *i-ML-Enc* with other methods in 9 performance metrics on USPS, FMNIST and COIL-20. Five methods for manifold learning: t-SNE and ML-Enc are compared for NLDR; three AE-based methods AE, ML-AE and TopoAE are compared for reconstructible manifold learning. Three methods for inverse models: INN (Nguyen et al., 2019), i-RevNet (Jacobsen et al., 2018), and i-ResNet (Behrmann et al., 2019) are compared for bijective property. The visualization of NLDR and its inverse process of *i-ML-Enc* are shown in Fig. 7, together with the NLDR results of t-SNE and ML-Enc. The target dimension for visualization

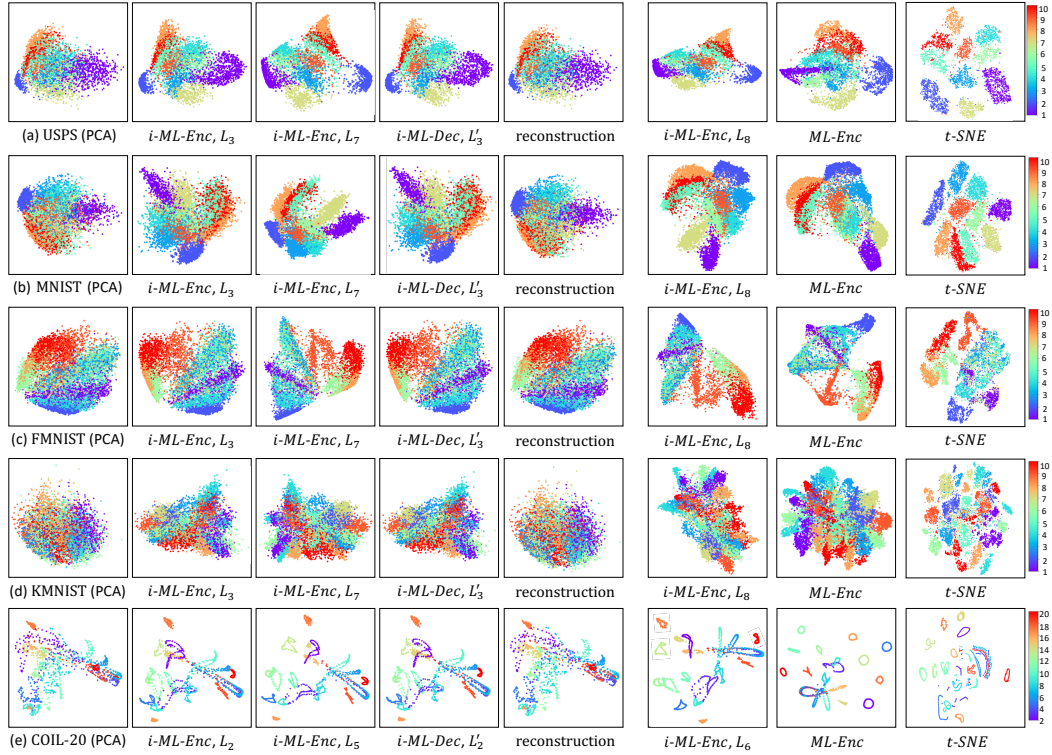


Figure 7: Visualization of invertible NLDR results of *i-ML-Enc* with comparison to ML-Enc and t-SNE on five real-world datasets. The target dimension $s' = 2$ for all datasets, and the high-dimensional latent space are visualized by PCA.

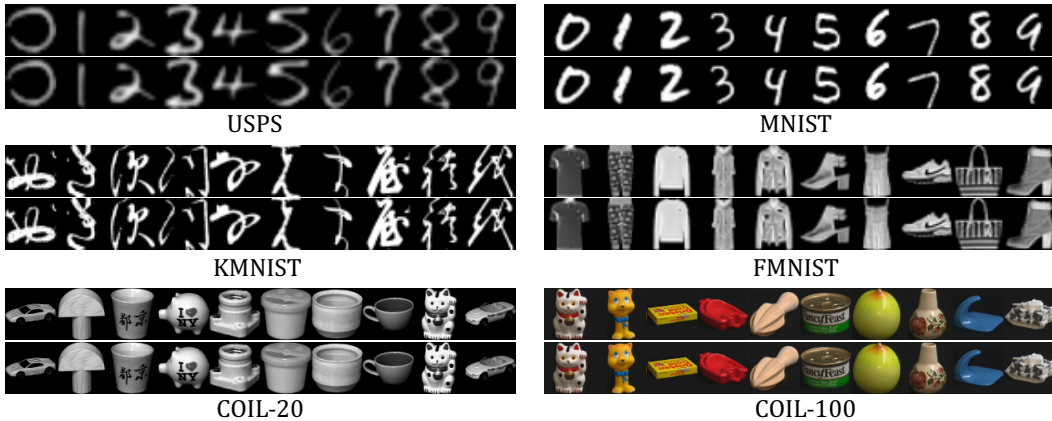


Figure 8: Visualization of reconstruction results of *i-ML-Enc* on six image datasets. For each cell, the upper row shows results of *i-ML-Enc* while the lower row shows the raw input images. As for COIL-20 and COIL-100, we randomly selected 10 classes to display.

is $s' = 2$ and the high-dimensional latent space are visualized by PCA. Compared with NLDR algorithms, the L -th layer of *i-ML-Enc* nearly achieves best NLDR results on FMNIST, but ranks the second place on USPS and the third place on COIL-20. Chances are that it is caused by the linear transformation layer, since the NLDR results of the $(L - 1)$ -th layer are quite reliable. Compared with other invertible models, *i-ML-Enc* outperforms in all the NLDR metrics and the RMSE loss, which shows the good quality of its low-dimensional representation of data manifolds with a series of equi-dimensional layers. Comparing the NME of *i-ML-Enc* with bijective models, *i-ML-Enc* has larger NME on FMNIST and COIL-20, which indicates that *i-ML-Enc* is more unstable dealing with

complex datasets. Besides, we visualize the reconstruction samples of six image datasets including COIL-100 (Nene et al., 1996a) to show the inverse quality of *i-ML-Enc* in Fig. 8.

A.3 LATENT SPACE INTERPOLATION

A.3.1 DATASETS COMPARISON

Here is a brief introduction to four interpolation data sets. We analyze the difficulty of dataset roughly according to **dimension**, **sample size**, **image entropy**, **texture**, and the performance of **classification tasks**: (1) Sampling ratio. The input dimension and sample number reflect the sampling ratio. Generally, the sample number has an exponential relationship with the input dimension in the case of sufficient sampling. Thus, the sampling ratio of USPS is higher than others. (2) Image entropy. The Shannon entropy of the histogram measures the information content of the image, and it reaches the maximum when the density estimated by histogram is an uniform distribution. We report the mean entropy of each dataset. We conclude that USPS has richer gray scale than MNIST(256), while the information content of MNIST(784), KMNIST and FMNIST shows an increasing trend. (3) Texture. The standard deviation (std) of the histogram reflects the texture information in the image, and we report the mean std of each dataset. Combined with the evaluation of human eyes, the texture features become more and more rough from USPS, MNIST to KMNIST, while FMNIST contains complex and regular texture. (4) Classification tasks. We report the mean accuracy of 10-fold cross validation using kNN and logistic classifier (Pedregosa et al., 2011) for each data set. The credibility of neighborhood system decreases gradually from USPS, MNIST, KMNIST to FMNIST. Combined with visualization results of each dataset in Fig. 7, it obvious that KMNIST has the worst linear separability. Above all, we can roughly give the order of the difficulty of manifold learning on each data set: **USPS<MNIST(256)<MNIST(784)<KMNIST<FMNIST**.

Table 5: Comparison of manifold learning difficulties of interpolation datasets

Dataset	Class	Train set	Dimension	Entropy	Texture	KNN	Logistic
USPS	10	9298	256	5.479	0.5097	0.9589	0.9381
MNIST(256)	10	9298	256	1.879	10.51	0.9493	0.9099
MNIST(784)	10	20000	784	1.598	39.75	0.9515	0.8943
KMNIST	10	20000	784	2.911	33.01	0.9141	0.6471
FMNIST	10	20000	784	4.115	24.75	0.8133	0.7984

A.3.2 MORE INTERPOLATION RESULTS

kNN interpolation. We verify the reliability of the low-dimensional representation by kNN interpolation. Comparing the results of different values of k , as shown in Fig. 9, we conclude that: (1) Because the high-dimensional latent space is still quite sparse, there are some noise caused by linear approximation on the latent results. The MSE loss and noises of the latent results is increasing with the expansion of the local neighborhood on the same dataset, reflecting the reliability of local neighborhood system. (2) In terms of the same sampling rate, the MSE loss and noises of the latent results grow from MNIST(784), KMNIST to FMNIST, which indicates that the confidence of the local homeomorphism property of the latent space decreases gradually on more difficult manifolds. (3) In terms of the similar data manifolds, USPS(256) and MNIST(256) show better latent interpolation results than MNIST(784), which demonstrates that it is harder to preserve the geometric properties on higher input dimension. (4) Though the latent results import some noise, the input results have unnatural transformation such as pseudo-contour and overlapping. Thus, the latent space results are more smooth than the input space, which validates that the latent space learned by *i-ML-Enc* is flatter and denser than the input space. In a nutshell, we infer that the difficulty of preserving the geometric properties based on approximation of the local tangent space by the local neighborhood is the key reason for the manifold learning fails in the real-world case.

Geodesic interpolation. We further perform the latent interpolation along the geodesic path between sample pairs when k is large to generate reliable intermediate samples. It might reflect the topological structure of data manifolds when two samples in a sample pair are in different clusters. Compared with results of MNIST, KMNIST and FMNIST, as shown in Fig. 10, we can conclude:

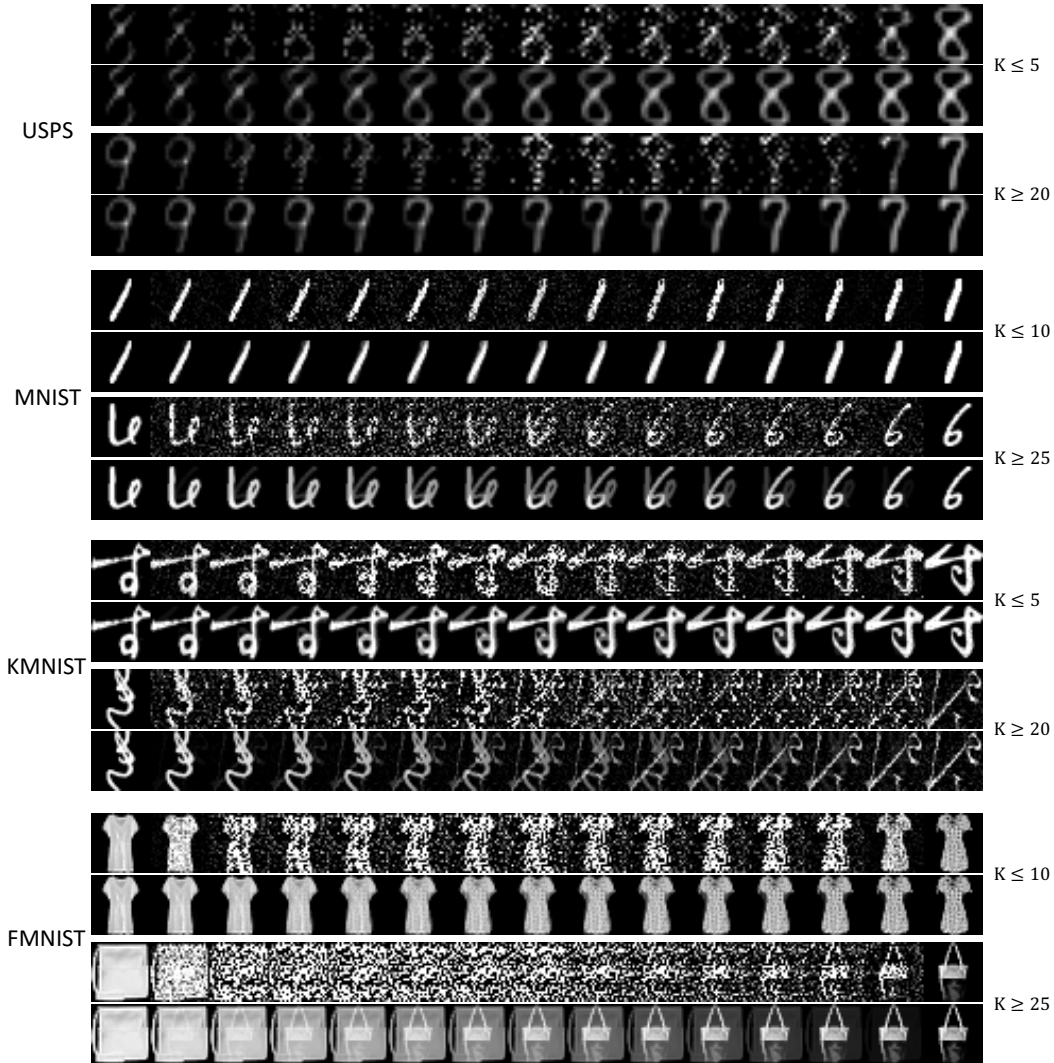


Figure 9: Visualization of kNN interpolation results of *i-ML-Enc* on image datasets with $k \leq 10$ and $k \geq 20$. For each row, the upper part shows results of *i-ML-Enc* while the lower part shows the raw input images. Both the input and latent results transform smoothly when k is small, while the latent results show more noise but less overlapping and pseudo-contour than the input results when k is large.

(1) The latent results is more reliable than that in the input space which can generates the synthetic samples between two different clusters. (2) Compared with MNIST, KMNIST and FMNIST, the latent results of more complex datasets are more ambiguous and noisy, which indicates that it is more difficult to find a low-dimensional representation of more complex data manifolds with all geometric structure preserved.

A.4 ABLATION STUDY

Analysis and conclusion. We further conduct ablation study of the *extra head* (+Ex), the orthogonal loss \mathcal{L}_{orth} (+Orth), and the zero padding loss \mathcal{L}_{pad} (+Pad) on MNIST, USPS, KMNIST, FMNIST and COIL-20. The Table 6 reports ablation results in the 8 indicators and the $r(Z^{L-1})$. We analyze and conclude: (1) The combination of **Ex** and **Orth** nearly achieve the best inverse and DR performance on MNIST, USPS, FMNIST and COIL-20, which indicates that it is the basic factor for invertible NLDR in the first $L - 1$ layers. (2) When only use **Orth**, the NLDR in the first $L - 1$ layer

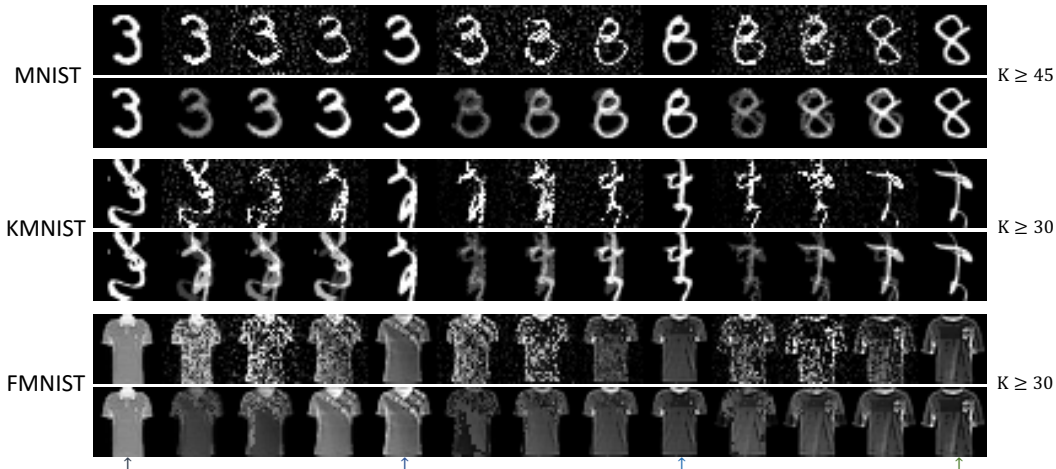


Figure 10: The interpolation results of the geodesic interpolation in the latent space. For each dataset, the upper row shows the latent result, while the lower shows the input result. The samples 1, 5, 9, 13 pointed by the arrow are the original samples.

of the network will degenerate into the identity mapping, and DR is achieved with linear project on layer L . (3) Combined with all three items **Ex**, **Orth** and **Pad**, *i-ML-Enc* obtains a sparse coordinate representation, but achieves little worse embedding quality on USPS and COIL-20 than using **Ex** and **Orth**. (4) Besides the proposed loss items, ML-AE overperforms the other combinations in the **Acc** metric indicating the reconstruction loss helps improve the generation ability of ML-Enc. Above all, the **Ex+Orth+Pad** combination, i.e. *i-ML-Enc*, can achieve the proposed invertible NLDR.

Further discussion. We notice that the s -sparse achieved by *i-ML-Enc* is higher than the approximate intrinsic dimension d on each dataset, e.g. 116-sparse on USPS and 125-sparse on MNIST. We found the following reasons: (1) Because the data manifolds are usually quite complex but sampling sparsely, the lowest isometric embedding dimension are between d to $2d$ according to Nash Embedding Theorem and the hyper-plane hypothesis. The s obtained by *i-ML-Enc* on each dataset is nearly failed into the region. (2) The proposed *i-ML-Enc* is not optimized enough which serves as a simple network implementation of inv-ML. We need to design a better implementation model if we want to approach the lower embedding dimension with the preservation of both geometry and topology.

Table 6: Ablation study of *i-ML-Enc* on five image datasets.

Dataset	Algorithm	RMSE	MNE	Trust	Cont	K min	K max	Acc	$r(Z^{L-1})$
MNIST	ML-AE	0.4012	16.84	0.9893	0.9926	1.704	57.48	0.9340	15
	ML-Enc	-	-	0.9862	0.9927	1.761	58.91	0.9326	14
	+Ex	-	-	0.9891	0.9812	2.745	78.88	0.9316	12
	+Ex+Orth	0.0341	0.4255	0.9874	0.9927	1.817	59.97	0.9298	361
	+Ex+Orth+Pad	0.0457	0.5085	0.9906	0.9912	2.033	60.14	0.9316	125
	+Orth	0.0056	0.1275	0.9652	0.9578	1.597	53.21	0.8807	716
USPS	ML-AE	0.4912	11.84	0.9879	0.9905	1.529	55.32	0.9576	16
	ML-Enc	-	-	0.9874	0.9897	1.562	52.14	0.9534	14
	+Ex	-	-	0.9849	0.9836	2.525	78.88	0.9413	11
	+Ex+Orth	0.0395	0.2511	0.9895	0.9875	1.366	58.83	0.9376	192
	+Ex+Orth+Pad	0.0253	0.3058	0.9886	0.9861	1.538	60.79	0.9456	116
	+Orth	0.0109	0.2043	0.9702	0.9654	1.328	66.25	0.8961	243
KMNIST	ML-AE	0.4912	18.84	0.9781	0.9912	2.478	80.66	0.7639	19
	ML-Enc	-	-	0.9738	0.9883	2.253	103.4	0.7719	18
	+Ex	-	-	0.9786	0.9801	5.826	255.1	0.7624	18
	+Ex+Orth	0.0463	0.4661	0.9805	0.9872	2.396	70.89	0.6325	406
	+Ex+Orth+Pad	0.0844	0.4589	0.9875	0.9894	2.697	78.19	0.7513	198
	+Orth	0.0223	0.1962	0.9621	0.9593	1.991	60.51	0.5922	732
FMNIST	ML-AE	0.4912	18.84	0.9912	0.9917	1.738	101.7	0.7665	19
	ML-Enc	-	-	0.9903	0.9896	1.358	89.65	0.7629	18
	+Ex	-	-	0.9886	0.9726	5.826	279.4	0.7624	16
	+Ex+Orth	0.0337	0.3194	0.9895	0.9840	1.879	98.66	0.7613	393
	+Ex+Orth+Pad	0.0461	0.3567	0.9923	0.9905	1.298	83.63	0.7644	182
	+Orth	0.0152	0.2975	0.9701	0.9593	2.073	89.03	0.5934	743
COIL-20	ML-AE	0.1220	16.87	0.9914	0.9885	1.489	74.79	0.9564	44
	ML-Enc	-	-	0.9920	0.9889	1.502	70.79	0.9564	46
	+Ex+Orth	0.0049	0.093	0.9927	0.9852	1.378	66.39	0.9427	1190
	+Ex+Orth+Pad	0.0171	1.026	0.9921	0.9871	1.695	71.86	0.9386	746